Journal of Magnetic Resonance 374 (2025) 107866

Contents lists available at ScienceDirect

Journal of Magnetic Resonance

journal homepage: www.elsevier.com/locate/jmr

Design of planar transmission line microwave probes for broadband EPR spectroscopy

Selina Eckel [a,*], Julian Nagel [a], Mazin Jouda [b], Jan Gerrit Korvink [b], Ahmet Çağrı Ulusoy [a]

[a] Institute of Radio Frequency Engineering and Electronics, Karlsruhe Institute of Technology, Karlsruhe, Germany
[b] Institute of Microstructure Technology, Karlsruhe Institute of Technology, Karlsruhe, Germany

ARTICLE INFO

Keywords:
Electron paramagnetic resonance
Broadband
Transmission lines
Microwave probe
Coplanar waveguide
Microstrip line

ABSTRACT

In broadband transmission-based electron paramagnetic resonance (EPR) spectrometers, non-resonant planar microwave probes play a key role, but very few systematic explorations of their design space exist. We develop design guidelines for two common types of transmission lines, microstrip and coplanar waveguide, to achieve a high effective microwave magnetic field strength, which ultimately leads to a more sensitive EPR measurement set-up. We compare the optimized transmission line structures and show that the coplanar waveguide achieves a higher simulated effective magnetic field strength. The simulation results are confirmed by EPR measurements up to a microwave frequency of 45 GHz.

1. Introduction

Electron paramagnetic resonance (EPR) spectrometers are used to study paramagnetic samples in a wide range of applications in biology, chemistry, and physics [1]. Conventional EPR spectrometers use resonators to generate a microwave magnetic field B_1 to excite the electron's spin in a sample, and to detect the EPR signal. Due to the typically narrow-band frequency range of resonators, the microwave frequency f_0 is kept constant while the external magnetic field B_0 is swept when performing EPR measurements. Resonators offer a high quality (Q)-factor and thus a high sensitivity, which is why they are widely used in EPR spectrometers. However, for less conventional materials with zero-field-splitting (ZFS), broad line shapes or numerous magnetic transitions, a broadband frequency-swept EPR measurement can offer unique information about the sample [2]. To build a broadband EPR spectrometer, a non-resonant inherently broadband planar transmission line can be used as the microwave probe. A transmission line generates a microwave magnetic field based on Ampere's law [3].

Several publications have already shown transmission line-based EPR measurements of Cr^{3+} atoms in a ruby single crystal, nitronyl-nitroxide radical [4–6], carbon fiber [6], DPPH powder [6–9], γ-irradiated fused silica [9], and dilute metal complexes [10–12]. In addition to demonstrating the feasibility of transmission line-based broadband EPR measurements, the mentioned references mainly focus on the EPR measurement architecture to improve the sensitivity, to realize pulsed EPR, or to perform cryogenic measurements. However, the design considerations for the transmission lines themselves and the choice of their design parameters are rarely discussed.

Table 1 gives an overview of the different types of transmission lines, orientations, substrates, and dimensions that have been used in the literature. Refs. [4–6] are from the same research group and use very similar transmission line structures. Ref. [9] places the sample in a cavity inside the substrate, in contrast to the other publications, where the sample is placed on top of the transmission lines. In [10,12], a wire is used as the conductor and is wound around a sample compartment while the other publications (and this work) use planar technologies that can be easily integrated with millimeter wave integrated circuits. No clear trend can be derived from the table as to which dimensions and properties the transmission line microwave probes should have. This paper aims to close this gap.

Transmission lines can be either used in reflection or transmission mode, but since the transmission mode does not require a circulator as an additional component in the set-up, we chose this mode of operation. We first develop design guidelines for the two common transmission line types, the microstrip (MS) and coplanar waveguide (CPW), to achieve a high magnetic field strength B_1, which leads to a higher energy absorption in the sample and thus to a higher EPR signal strength. For the optimization of the transmission line structures, we focus on their physical dimensions and the substrate properties. We also investigate the effect of the orientation of the transmission line w.r.t. the external magnetic field strength B_0. Based on the optimized transmission line structures we compare the simulated magnetic field strength B_1 of the two microwave transmission line types. In Section 3, we present the assembled transmission line structures and characterize

* Corresponding author.
E-mail address: selina.eckel@kit.edu (S. Eckel).

https://doi.org/10.1016/j.jmr.2025.107866
Received 18 December 2024; Received in revised form 20 February 2025; Accepted 3 March 2025
Available online 18 March 2025
1090-7807/© 2025 The Authors. Published by Elsevier Inc. This is an open access article under the CC BY license (http://creativecommons.org/licenses/by/4.0/).

Table 1
Overview of published transmission lines for EPR spectroscopy.

Ref.	Transmission line		Substrate			Dimensions		Frequency range	
	Type	Orientation	Material	ϵ_r	h	w	s	f_{min}	f_{max}
[4]	CPW	meander	Sapphire	10	0.33 mm	60 µm	25 µm	0.5 GHz	40 GHz
[5]	CPW	meander	Sapphire	10	0.43 mm	100 µm	41 µm	0.1 GHz	67 GHz
[6]	CPW	meander	Sapphire	10	0.43 mm	100 µm	42 µm	0.1 GHz	25 GHz
[7]	MS	meander	Silica	3.8	1.52 mm	100 µm	–	8.0 GHz	13 GHz
[8]	CPW	straight	RO4350	3.34	1.00 mm	150 µm	100 µm	1.0 GHz	15 GHz
[9][a]	MS	straight	n.A.	2	0.75 mm	1.92 mm	–	n.A.	n.A.
[10]	wire MS	meander	Acrylic tape	3.15	0.15 mm	0.25 mm	–	0.1 GHz	18 GHz

[a] Values extracted from supplementary material.

them by their transmission coefficient. In Section 4, we introduce our EPR measurement set-up and characterize the manufactured transmission line structures up to a microwave frequency of 45 GHz, which is mainly limited by the measurement set-up. Finally, we compare the EPR measurement results with the simulated magnetic field strength.

2. Optimization of the transmission line parameters

2.1. Theoretical background

EPR spectroscopy enables the study of the interaction energy of a paramagnetic sample in a static external magnetic field B_0, as described by the spin Hamiltonian [13]. One of the main interactions in EPR is the Electron-Zeeman effect, in which an unpaired electron interacts directly with the external magnetic field. Microwave power is absorbed by the sample at the resonance condition

$$\Delta E = g\mu_B B_0 = h f_0 \tag{1}$$

with the Zeeman energy gap ΔE, the g-factor g, the Bohr magneton μ_B, the external magnetic field B_0, the microwave frequency f_0, and Planck's constant h. Other interactions, such as the spin–spin or hyperfine interaction, lead to microwave absorption not only at the frequency f_0, but also at other frequencies [14].

The average power absorbed per unit volume p_{abs} is proportional to the square of the component $\vec{H}_1^{\perp}$ of the magnetic field strength $\vec{H}_1$ which is perpendicular to the external magnetic field B_0 [13]:

$$p_{abs} \propto \left|\vec{H}_1^{\perp}\right|^2 \tag{2}$$

Note that only one of the rotating components of a linearly polarized magnetic field H couples into the spin system and leads to a power absorption in the sample.

The magnetic field strength of transmission lines shows a strong spatial dependency and cannot be considered constant over the sample volume V_s. Therefore, the magnitude of the magnetic field strength needs to be integrated over the sample volume. This leads to the total power P_{abs} absorbed by the sample of:

$$P_{abs} = \iiint_{V_s} p_{abs}\mathrm{d}V \propto \iiint_{V_s} \left|\vec{H}_1^{\perp}(\vec{r})\right|^2 \mathrm{d}V. \tag{3}$$

Since the magnetic field distribution is uniform along the propagation direction of the transmission line, it is sufficient to integrate over the sample cross section A_s. In summary, the detected EPR voltage $V_{EPR} \propto \sqrt{P_{abs}}$ is proportional to the quantity

$$\sqrt{\iint_{A_s} \left|\vec{H}_1^{\perp}(\vec{r})\right|^2 \mathrm{d}A} =: H_A. \tag{4}$$

H_A captures the interaction between the magnetic field and the sample and can be interpreted as an "effective magnetic field strength", which can be directly related to the detected EPR voltage V_{EPR}. Due to the integration over the cross section, it has the unit of a current. This unit may seem uncommon, but we do not normalize H_A by the sample area because the total absorbed power (and thus V_{EPR}^2) is only proportional to the integrated square of the magnetic field (see Eq. (3)), which is assumed to be completely contained in the sample area. If we were to calculate an average/normalized effective magnetic field, this value would depend strongly on the somewhat arbitrary choice of a "large enough" integration area as the normalization constant.

The exact fields of planar transmission lines are a hybrid of transverse magnetic (TM) and transverse electric (TE) waves. For electrically very thin substrates (substrate height much smaller than the wavelength) the fields are quasi-transverse electromagnetic (TEM), which means that they are similar to the static case [3]. Unfortunately, there is no simple closed form expression to describe the fields of a planar transmission line [15].

For the MS transmission line, [16] derives the equations for the magnetic field strength under the assumption of a pure TEM wave. The author approximates the conductor as an array of line charges for which the electrical potential is calculated. The electric field is derived from the electrical potential and the magnetic potential is derived from the electric potential with the Cauchy–Riemann equations. For the CPW transmission line, [17] calculates the magnetic field by reducing the coupled slot-line problem to a rectangular waveguide problem by inserting appropriate electric and magnetic walls.

The derived equations from both references are still rather complicated and it is not directly evident how the magnetic field strength depends on the design parameters of the transmission lines. Therefore, the 3D finite element electromagnetic solver CST Microwave Studio is directly used to optimize the design parameters for the transmission lines. Since we assume a linear relation between H_1 and B_1 in the investigated paramagnetic sample, we use both H_1 and B_1 to describe the magnetic field.

As mentioned at the beginning of this section, only the components of the microwave magnetic field strength which are perpendicular to the external magnetic field B_0 contribute to the EPR signal. Fig. 1 shows the cross sections of the MS line and CPW. We define a local coordinate system (subscript "L") where the propagation direction of the transmission line is always oriented along the z_L-axis. The z-component of the magnetic field $\vec{H}_{1,z}$ can be neglected due to the nature of the quasi-TEM mode. Depending on the orientation of the transmission line w.r.t. the external magnetic field strength B_0 we can differentiate between two extreme cases, which are both realized and discussed in this paper:

1. $\vec{B}_0 \parallel \vec{e}_{z,L}$: The external magnetic field is pointing in the direction of propagation. In this case, both $H_{1,x}$ and $H_{1,y}$ contribute to the EPR signal and the magnitude of the magnetic field strength can be calculated as
$$\left|\vec{H}_1^{\perp}(\vec{r})\right| = \sqrt{H_{1,x}^2 + H_{1,y}^2}. \tag{5}$$
This case is relevant for the manufactured 90°-rotated structures (MS90 and CPW90, see Fig. 10) as discussed in Section 3.
2. $\vec{B}_0 \parallel \vec{e}_{x,L}$: The external magnetic field is oriented perpendicular to the direction of propagation, which results in the contribution of only $H_{1,y}$ to the EPR signal:
$$\left|\vec{H}_1^{\perp}(\vec{r})\right| = \sqrt{H_{1,y}^2} \tag{6}$$
This case is relevant for the manufactured straight structures (MS0 and CPW0, see Fig. 10) as discussed in Section 3.

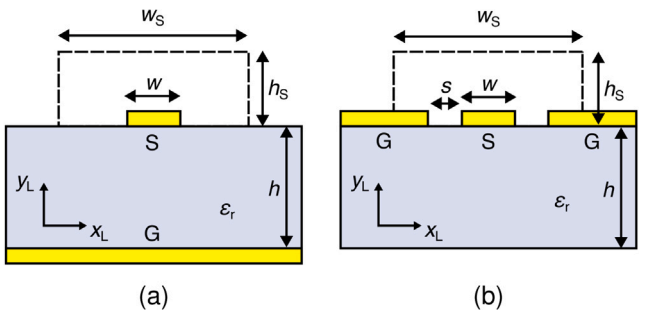

Fig. 1. Cross section in the $x_L y_L$-plane of (a) the MS line and (b) the CPW, with the conductor width w, the gap width s, the substrate height h, and the substrate dielectric constant ε_r. For both transmission lines, the signal line (S) is on top of the substrate. The ground plane (G) is on the bottom of the substrate for the MS transmission line and on the top of the substrate for the CPW transmission line. The dashed area indicates the sample cross section with width w_s and height h_s.

For the optimization of the design parameters of the individual transmission lines, we focus on the results based on the first case due to the similar spatial dependency of $H_{1,y}$ and $H_{1,x}$. The two cases are compared based on the optimized parameters in Section 2.4.

For the CST simulations, we approximate the cross section of the sample by a rectangle with the dimensions $w_s = 2500\,\mu m$ and $h_s = 300\,\mu m$. Those values are chosen sufficiently large to ensure that the magnetic field is contained within this cross section for the entire design space. Consequently, the optimized values are independent of the sample size, provided the sample size is not much smaller than the given values. In Section 5, we shortly discuss the choice of the design parameters for very small samples. Although the cross-section is not perfectly constant, the sample is so large that the areas in which the cross-section is not constant are negligible or very small.

Due to the model's linearity, the optimization of the design parameters does not depend on the specific value of the input power. For ease of presentation, the simulated values for the effective magnetic field strengths are shown for an input power of $P_{in} = 0.5\,W$. All transmission line structures are simulated with open boundaries in the x_L- and z_L-directions and with air above the transmission line in the positive y_L-direction. For the MS line, the boundary in the negative y_L-direction is set as electric, and for the coplanar waveguide transmission line it is set to open. We use a hexahedral mesh that is locally refined in the sample area to achieve a high magnetic field resolution.

2.2. Microstrip transmission line

A MS transmission line is mainly defined by its substrate height h, substrate dielectric constant ε_r and conductor width w, see Fig. 1(a). The signal line is located on top of the substrate and the ground plane is located on the bottom of the substrate. The dependency of the effective magnetic field strength H_A on the height of the substrate h for $\varepsilon_r = 9.9$ and $w = 235\,\mu m$ is shown in Fig. 2. It can be observed that the substrate height h has a minor influence on the effective magnetic field strength. The two smaller substrate heights show slightly higher values for higher frequencies.

To compare three common commercially available dielectric constants ε_r, we keep $h = 250\,\mu m$ and $w = 235\,\mu m$ constant. Materials with a dielectric constant of $\varepsilon_r = 3.38$, 6.15, and 9.9 include Rogers 4003C, Rogers 3006, and Alumina, respectively. As can be seen in Fig. 3, a higher dielectric constant ε_r leads to a higher effective magnetic field strength. The influence of the conductor width w can be seen in Fig. 4, where the other two parameters are chosen as $\varepsilon_r = 9.9$ and $h = 250\,\mu m$. With decreasing conductor width w, the effective magnetic field strength becomes larger.

For the measurements, the input signal of the transmission lines is provided by a $50\,\Omega$ commercial signal generator, and the structures are

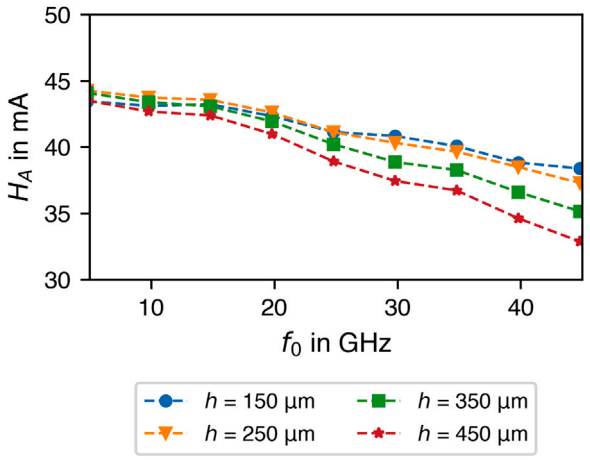

Fig. 2. Simulation results for the influence of different substrate heights h of a MS transmission line on the effective magnetic field strength H_A w.r.t. the microwave frequency f_0. The other design parameters are $w = 235\,\mu m$ and $\varepsilon_r = 9.9$. The height of the substrate h has a minor effect on the effective magnetic field strength.

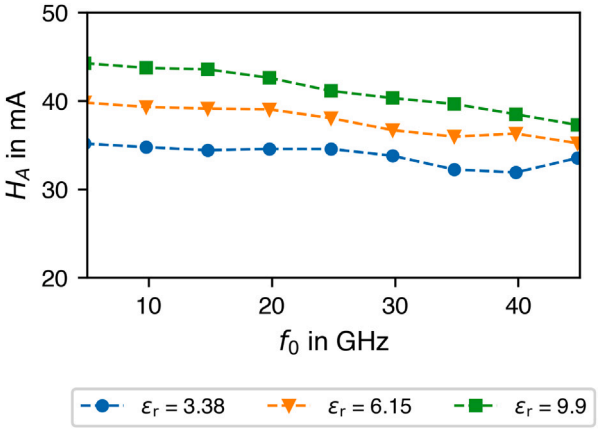

Fig. 3. Simulation results for the influence of different dielectric constants ε_r of a MS transmission line on the effective magnetic field strength H_A w.r.t. the microwave frequency f_0. The other design parameters are $w = 235\,\mu m$ and $h = 250\,\mu m$. A higher dielectric constant leads to a higher effective magnetic field strength.

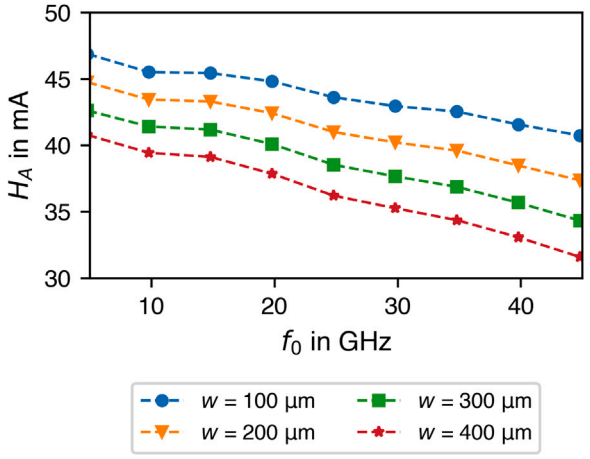

Fig. 4. Simulation results for the influence of different conductor widths w of a MS transmission line on the effective magnetic field strength H_A w.r.t. the microwave frequency f_0. The other design parameters are $\varepsilon_r = 9.9$ and $h = 250\,\mu m$. A smaller conductor width w leads to a higher effective magnetic field strength.

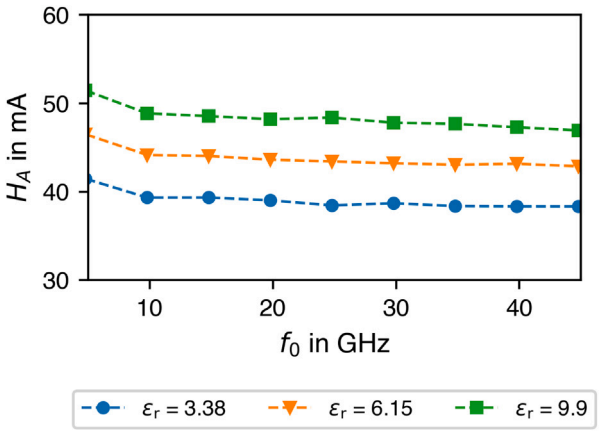

Fig. 5. Simulation results for the influence of the dielectric constants ε_r of a CPW transmission line on the effective magnetic field strength H_A w.r.t. the microwave frequency f_0. The other design parameters are $s = 110\,\mu m$, $w = 235\,\mu m$, and $h = 250\,\mu m$. A higher dielectric constant leads to a higher effective magnetic field strength.

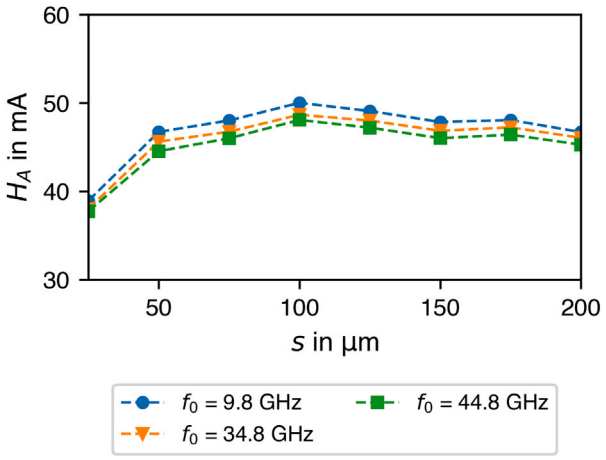

Fig. 6. Simulation results for the influence of the gap size s of a CPW transmission line on the effective magnetic field strength H_A. For each gap size s the conductor width w is adjusted to get an impedance of $Z_0 = 50\,\Omega$. The other design parameters are $\varepsilon_r = 9.9$ and $h = 250\,\mu m$. The optimum gap size is reached at approximately $s = 100\,\mu m$.

assembled using commercial 50 Ω connectors. To ensure optimal power delivery to the transmission line structures over a broad frequency range, a characteristic impedance of $Z_0 = 50\,\Omega$ is chosen for the transmission lines. This eliminates one degree of freedom from the three design parameters [3]. As shown above, a higher dielectric constant ε_r and a smaller conductor width w lead to higher effective magnetic field strengths. For a fixed characteristic impedance Z_0 and substrate height h, a higher dielectric constant ε_r leads to a smaller conductor width w, which both increase the effective magnetic field strength. Due to in-house manufacturing constrains, $h = 250\,\mu m$ was the smallest available substrate height for substrates with $\varepsilon_r = 9.9$. This limits the conductor width to $w = 235\,\mu m$.

2.3. Coplanar waveguide transmission line

The cross section of a CPW transmission line can be seen in Fig. 1(b). Compared to the MS transmission line, the signal and ground lines are on the same side of the substrate. A CPW transmission line is defined by the dielectric constant ε_r of the substrate, the conductor width w, and the gap between the conductor and the ground planes s. To a first approximation, the CPW transmission mode is independent of the substrate height h.

Similar to the MS transmission line, the effective microwave magnetic field increases with a higher dielectric constant ε_r, see Fig. 5. For the shown curves, the conductor width is chosen as $w = 235\,\mu m$ and the gap size as $s = 110\,\mu m$.

Fig. 6 shows the influence of the gap size s and conductor width w. For each gap size s the conductor width w is chosen so that the characteristic impedance is $Z_0 = 50\,\Omega$. For a dielectric constant of $\varepsilon_r = 9.9$, a characteristic impedance of $Z_0 = 50\,\Omega$ is achieved for $w \approx 2s$. The curves are shown for $f_0 = 9.8\,GHz$, $f_0 = 34.8\,GHz$, and $f_0 = 44.8\,GHz$, but the same trend is observable for all the other frequencies. It can be seen that smaller gap sizes (and smaller conductor widths) lead to a decreased effective magnetic field strength. The gap size s has a higher influence on the effective magnetic field strength than the conductor width w. For a gap size of approximately $s = 100\,\mu m$ the effective magnetic field strength reaches its maximum. The effective magnetic field strength decreases slightly for even higher gap sizes s.

In contrast to the MS transmission line, the width of the conductor w can be selected independently of the substrate height to achieve $Z_0 = 50\,\Omega$, since the characteristic impedance is approximately independent of the substrate height. For ease of manufacturing, a conductor width of $w = 235\,\mu m$ and a gap size of $s = 110\,\mu m$ is chosen. For the final CPW transmission line design, the smallest available substrate height of $h = 250\,\mu m$ is chosen to avoid substrate modes at higher frequencies [3].

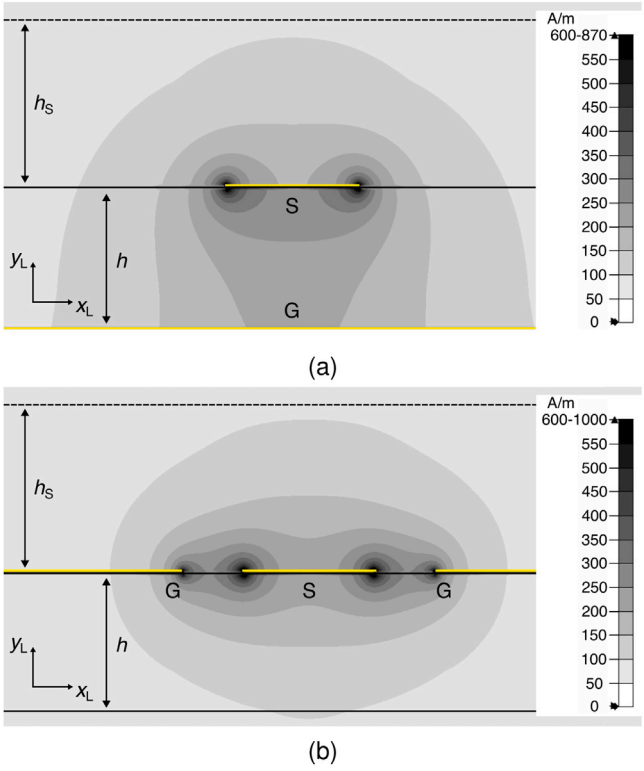

Fig. 7. Cross section in the $x_L y_L$-plane of the simulated magnetic field distribution at $f_0 = 9.8\,GHz$ for (a) the MS transmission line and (b) the CPW transmission line. The maximum field value is 870 A/m, and 1000 A/m, respectively, which appears in both cases at the edge of the signal line.

2.4. Comparison of MS and CPW transmission line

After optimizing each type of transmission line individually, their results are compared in this section. Fig. 7 shows the distribution of the magnetic field in the $x_L y_L$-cross section at $f_0 = 9.8\,GHz$.

To highlight their differences, Fig. 8 shows the lateral (along the x_L-axis) distribution of the magnetic field strength for both types of transmission line. It is calculated by integrating the magnetic field strength shown in Fig. 7 over the sample height $h_s = 300\,\mu m$.

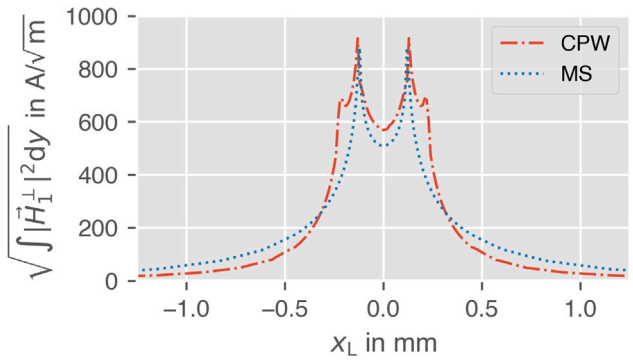

Fig. 8. Lateral distribution of the simulated effective magnetic field strength for the CPW and MS transmission line at $f_0 = 9.8\,\text{GHz}$.

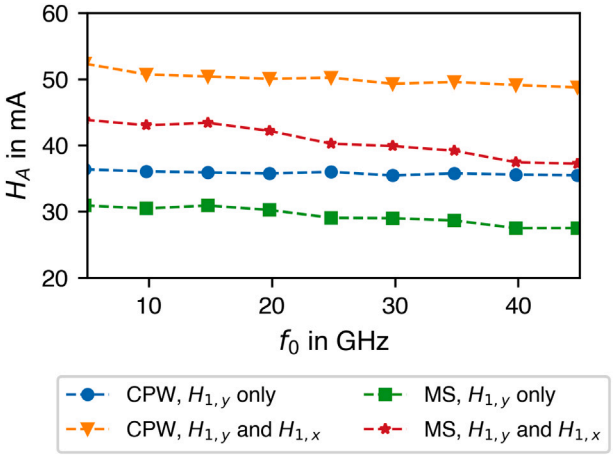

Fig. 9. Comparison of the simulated effective magnetic field strength H_A w.r.t. the microwave frequency f_0 for the CPW and MS transmission line. The different orientations of the external magnetic field strength B_0 w.r.t. the transmission lines is compared. "$H_{1,y}$ and $H_{1,x}$" corresponds to $\vec{B}_0 \parallel \vec{e}_{z,\text{L}}$, and "$H_{1,y}$ only" corresponds to $\vec{B}_0 \parallel \vec{e}_{x,\text{L}}$.

The maximum magnetic field strength is reached for both transmission line types at the edges of the conductor ($x_\text{L} \approx \pm 0.12\,\text{mm}$), while the CPW transmission line shows a slightly higher maximum value. The CPW transmission line shows a second peak at the edge of the ground line ($x_\text{L} \approx \pm 0.17\,\text{mm}$). Closer to the center of the conductor ($x_\text{L} = 0$), the CPW transmission line shows a higher magnetic field strength than the MS transmission line. The MS transmission line shows a higher magnetic field strength further away from the center of the conductor.

Integrating the lateral distribution of the magnetic field strength of Fig. 8 along the x-axis leads to the effective magnetic field strength H_A. Fig. 9 shows the effective magnetic field strength H_A of the MS and CPW transmission line for both cases of orientations of the transmission line w.r.t. to B_0 [see (5) and (6)], which are the four designs that are manufactured and characterized in Section 3.

It can be seen that for both orientations H_A is higher for the CPW transmission line than for its MS transmission line counterpart. Furthermore, it can be observed that when only $H_{1,y}$ contributes to the EPR signal, H_A is approximately 70% for both transmission line types. It is interesting to note that the MS transmission line with both $H_{1,y}$ and $H_{1,x}$ contributing to the EPR signal performs better than the CPW transmission line when only $H_{1,y}$ contributes to the EPR signal.

3. Assembly of test structures and electrical verification

To verify the simulated results shown in Fig. 9, four different transmission line structures are manufactured and assembled which can be seen in Fig. 10 from the top view. We introduce a second, global coordinate system (subscript "G") to describe the orientation of the transmission lines and the measurement set-up. The sample is placed in the center of the transmission lines, where the arrows indicate the direction of the microwave magnetic field, which corresponds to the x_L-axis of the local coordinate system. The orientation of the external magnetic field B_0 is also indicated in Fig. 10. For the 90°-rotated transmission lines in the lower half of the pictures (MS90, CPW90), both $H_{1,y}$ and $H_{1,x}$ contribute to the EPR signal and thus represent the first case, described in (5). For the straight transmission lines, shown in the upper half of the pictures (MS0, CPW0), only $H_{1,y}$ contributes to the EPR signal. For both orientations, the optimized parameters listed in Table 2 are used.

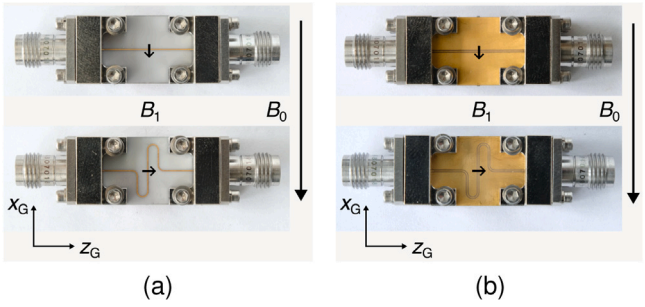

Fig. 10. Pictures of the MS (a) and CPW (b) transmission lines manufactured from gold-laminated Alumina. The upper pictures show the straight transmission lines (MS0 and CPW0) and the lower pictures show the 90° rotated transmission lines (MS90 and CPW90). The arrows in the center of the structure indicate the direction of the microwave magnetic field B_1 at the sample position. The transmission lines are assembled with 1.85 mm edge-launch connectors.

Table 2
Dimensions of the transmission line structures.

TL type	Substrate	w in µm	s in µm	h in µm
CPW	Alumina, $\varepsilon_r = 9.9$	235	110	250
MS	Alumina, $\varepsilon_r = 9.9$	235	–	250

Two-sided (one-sided) gold-laminated Alumina, with a dielectric constant of $\varepsilon_r = 9.9$, is used as the substrate for the MS (CPW) transmission line. The gold layer is approximately 3 µm thick. The outline of all the structures have the dimensions of $W = 12.7\,\text{mm}$, $L = 17.8\,\text{mm}$ (see Fig. 11), and were fabricated in-house with a LPKF ProtoLaser R4. They are assembled with 1.85 mm end-launch connectors which have a pin diameter of 0.13 mm and cover the frequency range up to 67 GHz.

The connectors will introduce unavoidable losses and ripples on the transmission coefficient S_{21}. To keep those effects to a minimum, we designed a transition structure for the MS transmission lines to convert the coplanar/coaxial mode of the connector to the desired microstrip mode, see Fig. 11. The signal line width is kept constant at $w = 235\,\mu\text{m}$ while the gap between the ground plane and the signal line is increased in positive z_G-direction. To keep the impedance mismatch to a minimum, the first via of the transition structure is placed as close as possible to the edge of the ground plane which is parallel to the signal line. For the CPW transmission line, the connector is directly attached without any specific transition structure. No major improvements are observed when tapering the signal or ground line to compensate for an impedance mismatch.

In order to suppress unwanted propagation modes, a 0.5 mm thick FR4 substrate is mounted under the Alumina substrate of the CPW. The FR4 substrate increases the distance from the bottom of the Alumina substrate and the bottom of the connector which acts as Ground. A 0.5 mm thick FR4 substrate is also mounted under the MS transmission line for mechanical stability. Note that this has the side effect that the ground of the MS transmission line is only connected with the ground of

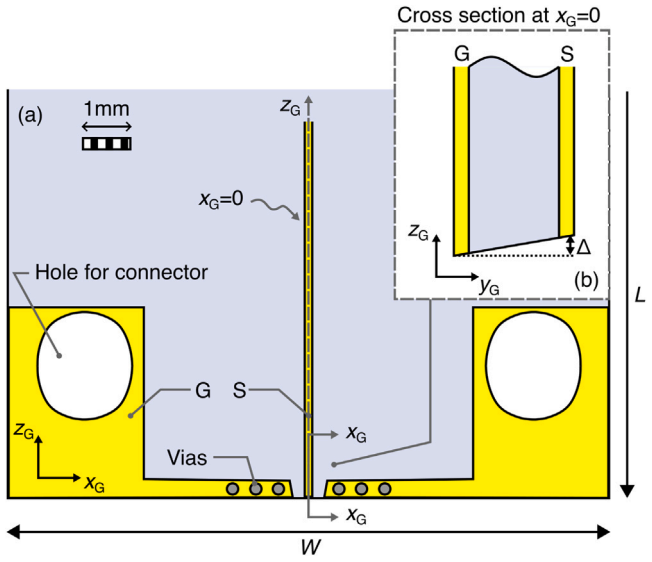

Fig. 11. In the main figure (a), the designed microstrip to connector transition in the $x_G z_G$-plane is shown. The inset (b) shows the structure in the $y_G z_G$-plane at position $x_G = 0$ to visualize the inclined edge of the board outline due to the manufacturing with the laser. The inclined edge leads to an unavoidable gap Δ between the connector and the board outline.

the connectors through the vias and at the sidewalls of the transmission line structure.

The measured magnitude of the transmission coefficient $|S_{21}|$ for all four structures can be seen in Fig. 12 (solid curves). The transmission lines rotated by 90° are longer than the straight lines and therefore show higher losses. Due to the cutting procedure of the Alumina substrate with a laser, the outer edge of the substrate is always slightly inclined, which leads to a gap between the connector and the Alumina board (see inset of Fig. 11). CST simulations confirm that a gap Δ in the order of hundred micrometers leads to increased losses at higher frequencies. By including the connectors, the FR4 substrates, a metal roughness of 2 µm, and a gap of 100 µm, we get the simulated transmission coefficient $|S_{21}|$ in Fig. 12 shown as dashed curves.

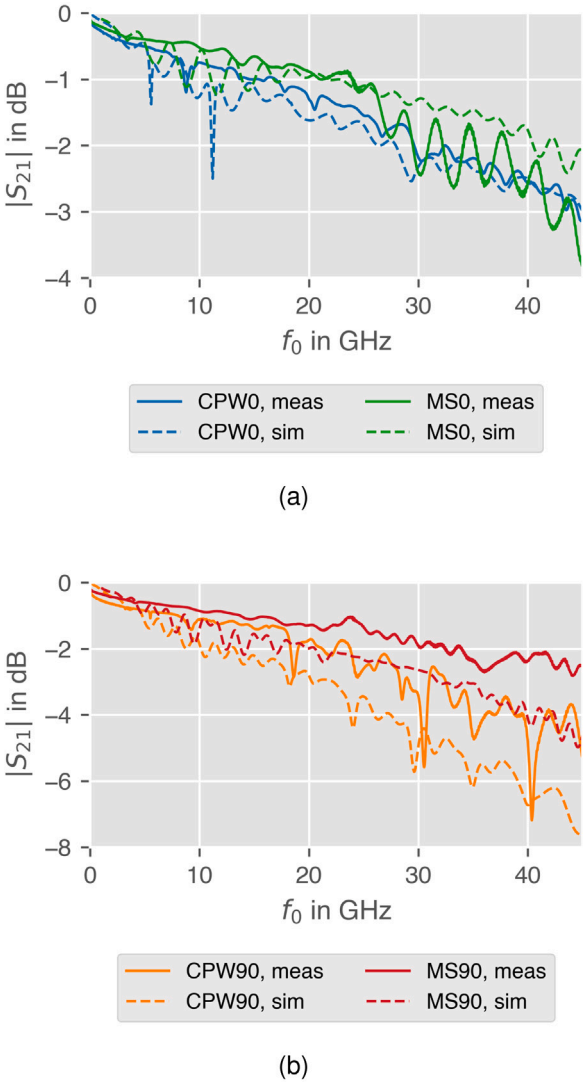

Fig. 12. Measured (solid curves) and simulated (dashed curves) transmission coefficient $|S_{21}|$ for (a) the straight transmission lines and (b) the 90°-rotated transmission lines.

4. Comparison of EPR measurements

4.1. EPR measurement set-up

To perform continuous-wave EPR measurements, the set-up shown in Fig. 13 is used. The generated microwave signal

$$s_0(t) = V_0 \cos(\omega_0 t) \tag{7}$$

with the microwave frequency $f_0 = \omega_0/(2\pi)$ and the amplitude V_0 is fed into the transmission line structure where the sample is located on top. The transmission line structure is placed inside a 3D-printed pair of Helmholtz coils, which is located inside an electromagnet, see Fig. 14. The electromagnet generates the external magnetic field B_0 and is driven by a 10 kW power supply. The external magnetic field B_0 is modulated by the modulation coils. The two coils of the Helmholtz pair have a radius R and are separated from each other by a distance $D = R = 16.8$ mm. Each coil has 100 windings, which results in a modulation amplitude of 0.4 mT/V. The modulation coil is driven by the output of the lock-in amplifier (LIA)

$$s_{\mathrm{LIA,out}}(t) = V_{\mathrm{m}} \cos(\omega_{\mathrm{m}} t) \tag{8}$$

with the modulation amplitude V_{m} and the modulation frequency $f_{\mathrm{m}} = \omega_{\mathrm{m}}/(2\pi)$. The signal $s_{\mathrm{LIA,out}}(t)$ is amplified by a factor of 50 by a high-voltage amplifier. The magnetic field strength is measured with a teslameter. By modulating the external magnetic field and thereby the strength of the EPR effect in the sample, the input signal $s_0(t)$ is amplitude modulated (AM). The AM signal is calculated to

$$s_{\mathrm{AM}}(t) = V_0 \cos(\omega_0 t) + \frac{mV_0}{2} \cos\left((\omega_0 + \omega_{\mathrm{m}})t\right) + \frac{mV_0}{2} \cos((\omega_0 - \omega_{\mathrm{m}})t). \tag{9}$$

The modulation index m is directly proportional to both the absorption of the EPR sample and the modulation amplitude V_{m}. The diode detector with its non-linear current–voltage curve demodulates the AM signal. The EPR information is solely contained in the signal component at the modulation frequency, which can be determined as

$$s_{\mathrm{dem}}(t) = \frac{V_0^2 G_{\mathrm{d}}' m}{2} \cos(\omega_{\mathrm{m}} t + \varphi_0) + (\ldots), \tag{10}$$

omitting terms with other mixing products. G_{d}' is the effective transconductance and φ_0 is the phase which is introduced by the phase offsets and propagation delays of the system components [18].

The lock-in amplifier downconverts the demodulated signal $s_{\mathrm{dem}}(t)$ with the modulation frequency f_{m} of the oscillator which leads to a downconversion of the EPR signal to direct current (DC). This allows the use of a narrow adaptive low-pass filter with a low cut-off frequency

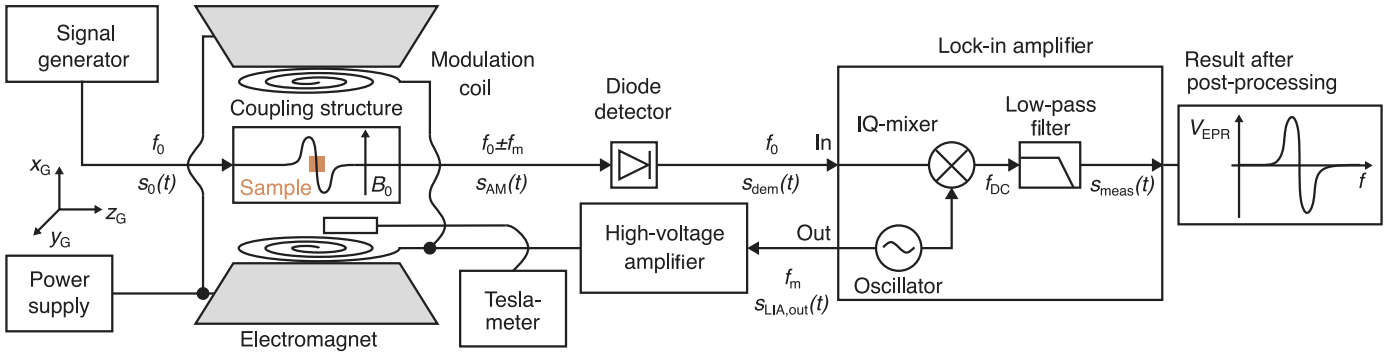

Fig. 13. Block diagram of the transmission-based EPR measurement set-up after [19]. At each stage, the present signals and their relevant frequency components are annotated. The sample is placed on top of the microwave transmission line structure which is placed inside the modulation coils and the electromagnet.

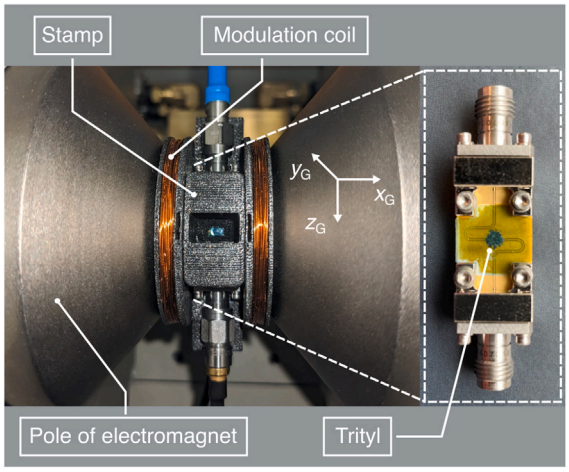

Fig. 14. Picture of the microwave transmission line placed inside the 3D-printed modulation coil which is fixed between the poles of the electromagnet. The sample is placed between a thin kapton (yellow color) and adhesion (blue color) foil and the sample is pressed on the microwave transmission line structure with a 3D-printed stamp (for more details see Fig. 15). Note, that the coordinate system is 90° rotated compared to Fig. 13.

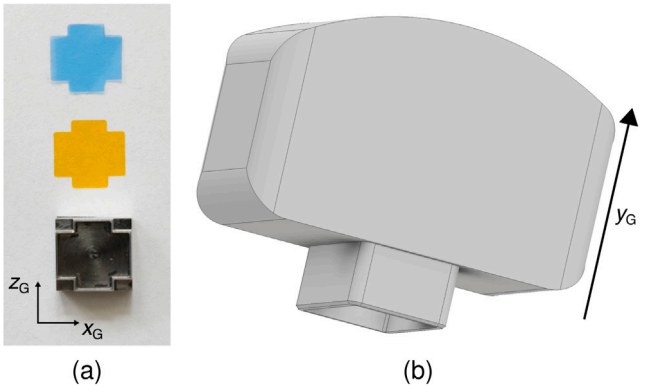

Fig. 15. (a) shows a picture of the components of the sample holder which ensure reproducible sample positioning in xz-direction. The sample is placed between a 12.5 µm thin kapton foil (yellow) and an adhesion foil (blue). The two foils are cut out with a cutter shown at the bottom of the picture. (b) shows the 3D-model of the stamp which ensures reproducible sample positioning in y-direction.

Table 3
Overview of the instruments used in the EPR measurement set-up.

Instrument	Name (Company)
Signal generator	E8257D PSG Analog Signal Generator (Keysight Technologies)
Electromagnet	5405 Electromagnet (GMW Associates)
Power supply	NGPS-100-100 (CAEN ELS s.r.l.)
Lock-in amplifier	MFLI 5 MHz Lock-In Amplifier (Zurich Instruments)
High-voltage amplifier	WMA-300 (Falco Systems)
Teslameter	Teslameter FM 302 (Projekt Elektronik GmbH)
Diode detector	33330C Coaxial Detector (Keysight Technologies)

leading to a high signal to noise ratio (SNR) [20]. Note that the lock-in principle is ultimately enabled by the modulated external magnetic field. The signal at the output of the lock-in amplifier can be described in its vector representation as

$$s_{meas}(f_0) = V_{meas}(f_0) \cdot \exp(j\varphi_{meas}(f_0)). \tag{11}$$

In our previous work [19], we show that there is an unwanted interference path present in the measurement set-up due to the combined use of the external magnetic field modulation and the planar transmission line structure. This leads to

$$s_{meas}(f_0) = V_{intf} \cdot \exp(j\varphi_{intf}) + V_{EPR}(f_0) \cdot \exp(j\varphi_{EPR}) \tag{12}$$

with V_{intf} and φ_{intf} being the amplitude and phase of the interference signal and V_{EPR} and φ_{EPR} being the amplitude and phase of the desired EPR signal. In the measured frequency range, only V_{EPR} dependents on the frequency. We introduce a post-processing scheme which involves the elimination of the interference signal before calculating the absolute value of the desired EPR signal $V_{EPR}(f_0)$. The EPR measurement results shown in this paper are obtained by applying this post-processing scheme.

The measurement instruments used in the set-up are listed in Table 3. The maximum possible frequency of the measurement set-up is 50 GHz, which is limited by the maximum operation frequency of the diode detector. The electromagnet can reach up to 2 T, which corresponds to a resonance microwave frequency of approximately 56 GHz according to (1). To achieve the fairest possible comparison between the transmission line structures, great care is required regarding sample handling and positioning. The sample in powder form is placed between a 12.5 µm thin kapton foil (yellow) and an adhesion foil (blue). To ensure a repeatable sample position in x_G- and z_G-direction, the foils are cut out with an in-house manufactured cutter to fit exactly between the connectors, see Fig. 15(a). With a 3D-printed stamp (see Fig. 15(b)) the sample is pressed onto the transmission line structure to ensure a constant sample position in y_G-direction. The bottom of the stamp has a hollow rectangular outline which is the only contact point on the sample holder to ensure that the sample is not compressed.

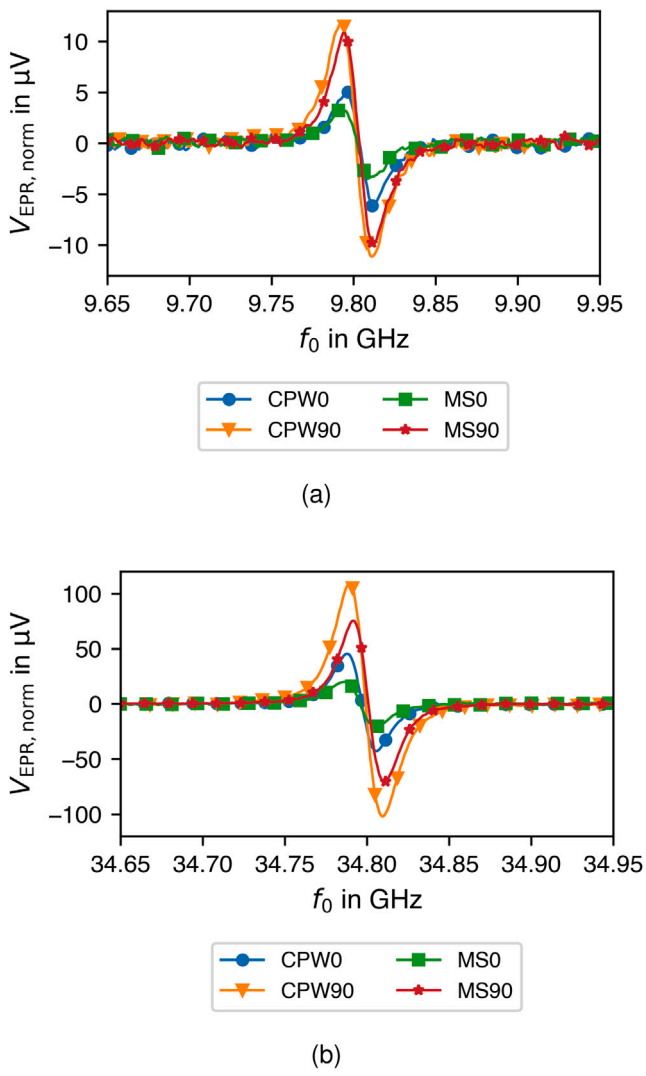

Fig. 16. Measured EPR curves at the EPR resonance frequency (a) $f_{0,res} = 9.8\,\text{GHz}$ ($B_{0,res} = 350\,\text{mT}$) and (b) $f_{0,res} = 34.8\,\text{GHz}$ ($B_{0,res} = 1243.2\,\text{mT}$) for the microwave transmission lines shown in Fig. 10. The microwave frequency f_0 is swept and the external magnetic field B_0 is kept constant.

4.2. EPR measurement results

As mentioned in the introduction, the magnetic moment of the electron cannot only be influenced by the external magnetic field strength, but also by its atomic environment. Depending on the sample, the EPR spectrum can consist of several peaks, which can make its interpretation quite complex. In this paper, we use the sample Trityl in powder form, which has only one unpaired electron which is mainly influenced by the external magnetic field B_0 and thus shows only one EPR peak in the spectrum.

The EPR measurements are performed at different frequency ranges with EPR resonance frequencies from 4.8 GHz up to 44.8 GHz in 5 GHz steps. The microwave frequency f_0 is swept while the external magnetic field strength B_0 is kept constant. Fig. 16 exemplarily shows the normalized EPR signal amplitude $V_{EPR,norm}$ for the commonly used EPR frequency bands X- and Q-Band. For Fig. 16(a), the external magnetic field strength is set to $B_{0,res} = 350\,\text{mT}$ and, as expected based on (1), the EPR resonance frequency is at $f_{0,res} = 9.8\,\text{GHz}$. For Fig. 16(b), the external magnetic field is set to $B_{0,res} = 1243.2\,\text{mT}$ and the EPR curves show a zero-crossing again at the expected resonance frequency of $f_{0,res} = 34.8\,\text{GHz}$. The plots show approximately the gradient of the absorption curve, which leads to a first derivative profile due to the modulation of the external magnetic field B_0 [1]. All curves consist of 512 data points, but for better readability, only a few are indicated. The EPR signal amplitude V_{EPR} is normalized by the losses of the transmission lines

$$V_{EPR,norm} = \frac{V_{EPR}}{|S_{21}|}, \tag{13}$$

where $|S_{21}|$ is extracted from the measured data of Fig. 12. This allows us to only focus on the effect of the different transmission line types and not on the effect of the impedance mismatch and losses introduced by the connectors. Note that by mounting the transmission line structures several times into the measurement set-up, the actual losses for each transmission line can be slightly shifted along the frequency axis compared to the measurement results in Fig. 12. As a result, the normalization compensates for the general trend of the losses, but it is possible that slightly frequency-shifted effects are not taken into account.

To compare different EPR curves, the signal intensity is often used due to its proportionality to the concentration of unpaired electrons in a sample. The EPR signal intensity can be calculated as the double integral of the normalized EPR signal amplitude $V_{EPR,norm}$

$$\text{Signal intensity} = \iint V_{EPR,norm}\,\mathrm{d}f_0\,\mathrm{d}f_0 \tag{14}$$

which is equivalent to the area under the absorption curve. If the profile of the EPR curves remains constant, one can compare the EPR peak-to-peak derivative line amplitude $V_{EPR,norm,pp}$ [1].

For every EPR sample, measurement parameters such as the input power P_{in} of the signal generator, the modulation amplitude V_m, the modulation frequency f_m for driving the modulation coil, and the time constant τ (or 3 dB filter bandwidth) of the low-pass filter of the lock-in amplifier need to be determined.

The EPR signal intensity increases for lower input power levels with the square root of the input power. At higher input power levels, the signal intensity grows more slowly or becomes smaller, which is called saturation [21]. The signal intensity saturates because the population of the electron spin states at the lower and the higher energy level becomes equal. The input power P_{in} of the signal generator needs to be optimized to achieve the highest possible SNR while avoiding saturation which can lead to a distortion of the EPR lineshape [1]. For the following measurement results, P_{in} is adjusted for each frequency point such that the power at the input of the diode detector is constant at 3 dBm when the transmission line structure is replaced by a direct connection. This effectively removes the cable losses.

A higher modulation amplitude V_m increases the peak-to-peak derivative line amplitude $V_{EPR,pp}$ but may also lead to distortions of the lineshape of the EPR signal. If the modulation amplitude V_m is chosen too high, the signal intensity eventually decreases. We choose a modulation amplitude of $V_m = 0.4\,\text{V}$ to maximize the signal intensity without distorting the signal. We select a modulation frequency of $f_m = 20\,\text{kHz}$ to still be able to measure the modulation amplitude B_m with the teslameter.

The time constant τ of the low pass filter of the lock-in amplifier determines the noise in the spectrum. A higher time constant filters out noise leading to a higher SNR, but if it is chosen too long compared to the frequency sweep time (in our case 45 s) the signal can be distorted or even missed [21]. We choose a time constant of $\tau = 75\,\text{ms}$ to avoid distortion while ensuring a high SNR.

Note that the baseline noise in the presented EPR measurement curves mostly results from random external interference around the modulation frequency which is expected (and experimentally verified) to be independent of the transmission line microwave probes. Improving this noise floor by carefully tuning aspects of the set-up (such as shielding) is certainly possible. However, these are not the focus of this investigation, and since they do not affect the results of the presented

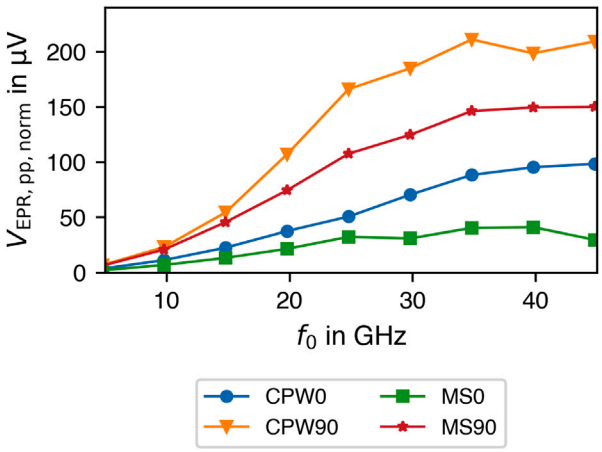

Fig. 17. Comparison of the normalized EPR peak-to-peak derivative line amplitude w.r.t. the microwave frequency f_0 for the different microwave transmission line structures.

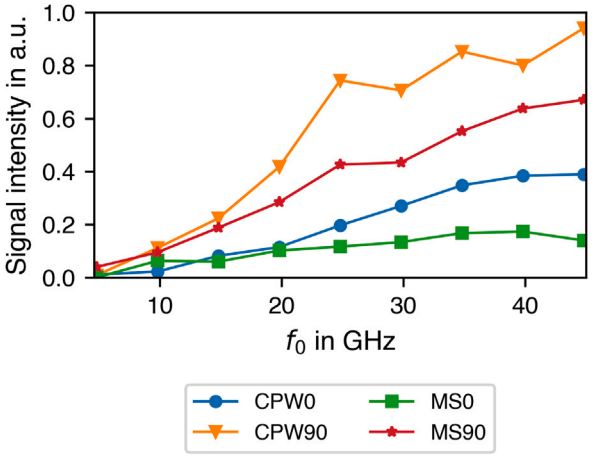

Fig. 18. Comparison of the signal intensity (double integral of the EPR curves) w.r.t. the microwave frequency f_0 for the different microwave transmission line structures.

relative comparisons, we only focus on the EPR signal amplitude as a good indicator of the overall SNR.

To investigate the behavior of the transmission line microwave probes themselves in the magnetic field (background measurements), we performed measurements without anything on top of the transmission line microwave probes. To check if the sample holder shows an EPR signal, we performed measurements with the empty sample holder on top of the transmission line microwave probes. In the measured frequency ranges, there was neither a background signal observable, nor an EPR signal from the empty sample holder.

To compare the different transmission line structures over the whole frequency band, we first compare the normalized EPR peak-to-peak derivative line amplitude $V_{EPR,norm,pp}$ in Fig. 17. Comparing the different transmission line types, the same trend as in the simulated effective magnetic field values H_A (see Fig. 9) is visible. The CPW90 structure (both $H_{1,y}$ and $H_{1,x}$ contribute to the EPR signal) shows the strongest EPR signal. It is possible to measure EPR signals with the straight transmission lines (only $H_{1,y}$ contributes to the EPR signal), but their EPR signal amplitude is proportionally even lower compared to the 90°-rotated structures than the simulation suggests.

As expected by (1), the normalized peak-to-peak EPR amplitude increases with higher microwave frequencies (and higher external magnetic field strengths) due to the increasing energy gap between the two spin states. Starting at around 25 GHz, a saturation effect becomes visible. The normalization of the curves with $|S_{21}|$ mainly corrects the higher losses of the CPW90 transmission lines for higher frequencies and the dip at f_0 = 29.8 GHz for the MS0 transmission line, see Fig. 12(a).

In Fig. 18, we also compare the signal intensity of the different EPR curves obtained by calculating the double integral of the normalized EPR amplitude, see (14), shown in Fig. 16. The same overall trend as in Fig. 17 can be seen with the CPW90 structure showing the highest values.

There are two anomalies in the shown signal intensity curves. First, the MS0 structure shows a higher value at 9.8 GHz than the CPW0 transmission line. Second, the CPW90 shows a dip at 30 GHz and 40 GHz. One reason for this effect is a not ideally flat baseline of the EPR curves. In commercial EPR spectrometers, there are semi-manual algorithms available to correct the baseline [21], but here only the raw data is shown. In addition, the transmission coefficient S_{21} of the CPW90 structure shows a dip close to 29.8 GHz and 39.8 GHz. By mounting the transmission line structures several times in the measurement set-up, it is possible that those dips shift slightly on the frequency axis and influence the EPR measurements at 29.8 GHz and 39.8 GHz.

5. Conclusion

In this paper, we have developed design guidelines for CPW and MS transmission lines to achieve a high effective magnetic field strength. For both transmission line types, a higher dielectric constant leads to a higher effective magnetic field strength. When designing a MS transmission line, a smaller conductor width leads to a higher effective magnetic field strength. The height of the substrate of a MS line has a minor influence on the effective magnetic field strength. For a CPW transmission line, the gap size has a higher influence on the effective magnetic field strength than the conductor width. The effective magnetic field strength first increases with larger gap sizes and then reaches a maximum.

Using samples much smaller than the sample area specified in Section 2.1, one has to ensure that the peaks of the magnetic field, which appear at the edges of the conductor, are within the sample area. Since a smaller conductor width of the MS transmission line leads to a higher effective magnetic field strength, the given value set is also optimum for smaller samples. For the CPW transmission line, the maximum magnetic field strength is higher for smaller gap sizes, which might be beneficial for very small samples. In this case, the sample placement plays an even bigger role because the sample would have to be placed exactly on the edge of the conductor line.

Each optimized transmission line type was fabricated in two different orientations. For the structures MS90 and CPW90 both microwave magnetic field components $H_{1,y}$ and $H_{1,x}$ are perpendicular to the external magnetic field B_0, whereas for the structures MS0 and CPW0 only $H_{1,y}$ is perpendicular to B_0. By considering the correct magnetic field components for each structure in the 3D-EM simulations, we have shown that it is possible to predict the relative performance of the transmission line structures used in EPR measurements. The CPW transmission line structures show a higher measured EPR peak-to-peak derivative line amplitude and signal intensity compared to the MS line counterparts. The 90°-rotated (MS90 and CPW90) structures lead to higher effective magnetic field strength than the straight (MS0 and CPW0) structures. In addition, the MS90 structure achieves a higher effective magnetic field strength than the CPW0 structure. A straight transmission line structure combined with a smaller connector might be useful if the space between the poles of the electromagnet is limited.

Although the CPW90 transmission line achieves a higher effective magnetic field strength, it also shows more ripples in $|S_{21}|$. For EPR samples with a higher spin state, and thus more EPR peaks, a wider frequency sweep range with the flattest possible $|S_{21}|$ curve is necessary to measure all the EPR peaks correctly (in the range of single-digit GHz instead of MHz). In this case, the MS90 transmission line might be more suitable than the CPW90 transmission line.

CRediT authorship contribution statement

Selina Eckel: Writing – original draft, Visualization, Validation, Methodology, Investigation, Formal analysis, Data curation, Conceptualization. **Julian Nagel:** Writing – review & editing, Visualization, Methodology, Investigation. **Mazin Jouda:** Writing – review & editing, Methodology. **Jan Gerrit Korvink:** Writing – review & editing, Project administration, Funding acquisition. **Ahmet Çağrı Ulusoy:** Writing – review & editing, Supervision, Project administration, Funding acquisition.

Declaration of competing interest

The authors declare that they have no known competing financial interests or personal relationships that could have appeared to influence the work reported in this paper.

Acknowledgments

We thank Andreas Lipp, Jonas Schwende, and Andreas Gallego for helping setting up the EPR measurement set-up, Mirko Nonnemacher for manufacturing the cutter for the sample holder, and Guinevere Mathies and Sanjay Vinod Kumar for providing the sample. The authors would like to thank the German Research Foundation (DFG) for its funding within the Collaborative Research Center 1527 "High Performance Compact Magnetic Resonance" (HyPERiON).

Data availability

Data will be made available on request.

References

[1] V. Chechik, E. Carter, D. Murphy, Electron Paramagnetic Resonance, Oxford University Press, USA, 2016.
[2] S.K. Misra, Multifrequency electron paramagnetic resonance, 2019.
[3] D.M. Pozar, Microwave Engineering: Theory and Techniques, John Wiley & Sons, 2021.
[4] C. Clauss, D. Bothner, D. Koelle, R. Kleiner, L. Bogani, M. Scheffler, M. Dressel, Broadband electron spin resonance from 500 MHz to 40 GHz using superconducting coplanar waveguides, Appl. Phys. Lett. 102 (16) (2013).
[5] Y. Wiemann, J. Simmendinger, C. Clauss, L. Bogani, D. Bothner, D. Koelle, R. Kleiner, M. Dressel, M. Scheffler, Observing electron spin resonance between 0.1 and 67 GHz at temperatures between 50 mK and 300 K using broadband metallic coplanar waveguides, Appl. Phys. Lett. 106 (2015) http://dx.doi.org/10.1063/1.4921231.
[6] B. Miksch, M. Dressel, M. Scheffler, Cryogenic frequency-domain electron spin resonance spectrometer based on coplanar waveguides and field modulation, Rev. Sci. Instrum. 91 (2020) http://dx.doi.org/10.1063/1.5141461.
[7] Z. Chen, J. Sun, P. Wang, Broadband ESR spectroscopy with a tunable interferometer, IEEE Trans. Magn. 53 (8) (2017) 1–9.
[8] K. Jing, Z. Lan, Z. Shi, S. Mu, X. Qin, X. Rong, J. Du, Broadband electron paramagnetic resonance spectrometer from 1 to 15 GHz using metallic coplanar waveguide, Rev. Sci. Instrum. 90 (12) (2019).
[9] P.R. Shrestha, N. Abhyankar, M.A. Anders, K.P. Cheung, R. Gougelet, J.T. Ryan, V. Szalai, J.P. Campbell, Nonresonant transmission line probe for sensitive interferometric electron spin resonance detection, Anal. Chem. 91 (17) (2019) 11108–11115.
[10] W.R. Hagen, Conversion of a single-frequency X-band EPR spectrometer into a broadband multi-frequency 0.1–18 GHz instrument for analysis of complex molecular spin Hamiltonians, Molecules 28 (13) (2023) 5281.
[11] W.R. Hagen, Broadband transmission EPR spectroscopy, PLoS One 8 (3) (2013) e59874.
[12] W.R. Hagen, Broadband tunable electron paramagnetic resonance spectroscopy of dilute metal complexes, J. Phys. Chem. A 123 (32) (2019) 6986–6995.
[13] C. Poole, Electron Spin Resonance: A Comprehensive Treatise on Experimental Techniques, in: Dover Books on Physics, Dover Publications, 1996.
[14] J.A. Weil, J.R. Bolton, Electron Paramagnetic Resonance: Elementary Theory and Practical Applications, John Wiley & Sons, 2007.
[15] R.E. Collin, Foundations for Microwave Engineering, John Wiley & Sons, 2007.
[16] W. Wiesbeck, Stromverteilung und Hochfrequenzeigenschaften der ungeschirmten Streifenleitung (Ph.D. thesis), 1972.
[17] R. Simons, R. Arora, Coupled slot line field components, IEEE Trans. Microw. Theory Tech. 30 (7) (1982) 1094–1099.
[18] U. Tietze, C. Schenk, E. Gamm, Halbleiter-Schaltungstechnik, sixteenth ed., Springer Vieweg, 2019.
[19] S. Eckel, A.C. Ulusoy, Post-processing scheme for EPR spectroscopy based on planar microwave structures, in: 2024 54th European Microwave Conference, EuMC, 2024, pp. 309–312.
[20] White Paper: Principles of Lock-In Detection and the State of the Art, Tech. Rep., Zurich Instruments, 2023, URL https://www.zhinst.com/sites/default/files/documents/2023-04/zi_whitepaper_principles_of_lock-in_detection_0.pdf.
[21] G. Eaton, S. Eaton, D. Barr, R. Weber, Quantitative EPR, Springer Vienna, 2010.